Granular elasticity: Stress distributions in silos and under point loads

Kurt Bräuer,[1] Michael Pfitzner,[2] Dmitry O. Krimer,[1] Michael Mayer,[1] Yimin Jiang,[3,1] and Mario Liu[1]
[1]*Theoretische Physik, Universität Tübingen,72076 Tübingen, Germany*
[2]*Universität der Bundeswehr München, 85579 Munich, Germany*
[3]*School of Physics Science and Technology and State Key Laboratory for Powder Metallurgy, Central South University, Changsha 410083, China*

(Received 27 March 2006; revised manuscript received 29 June 2006; published 27 December 2006)

An elastic-strain–stress relation, the result of *granular elasticity* as introduced in the preceding paper, is employed here to calculate the stress distribution (a) in cylindrical silos and (b) under point loads assuming uniform density. In silos, the ratio k_J between the horizontal and vertical stress is found to be constant (as conjectured by Janssen) and given as $k_J=1-\sin\varphi$ (with φ the Coulomb yield angle), in agreement with a construction industry standard usually referred to as the Jaky formula. Next, the stress distribution at the bottom of a granular layer exposed to a point force at its top is calculated. The results include both vertical and oblique point forces, which agree well with simulations and experiments using rainlike preparation. Moreover, the stress distribution of a sheared granular layer exposed to the same point force is calculated and again found in agreement with given data.

DOI: 10.1103/PhysRevE.74.061311 PACS number(s): 45.70.Cc, 81.05.Rm, 81.40.Jj

I. INTRODUCTION

In elastic media, the energy $w=w(\varepsilon_{ij})$ is a function of the strain ε_{ij}, a parametrization of the medium's deformation. Its derivative yields the stress-strain relation, $\sigma_{ij}=-\partial w/\partial\varepsilon_{ij}$, which is pivotal in closing the force balance, $\nabla_j\sigma_{ij}=0$, and enables us to determine stress distributions systematically, for any geometry and boundary conditions. In sand, the strain field $\varepsilon_{ij}=u_{ij}+u_{ij}^p$ has two parts: the elastic one that accounts for the deformation of the grains, and the plastic one for their irreversible rolling and slippage, with the latter usually dominating. This appears quite unfortunate, because the plastic contribution precludes a unique stress-strain relation, $\sigma_{ij}=\sigma_{ij}(\varepsilon_{k\ell})$. This is what makes granular stress calculation the notoriously open problem it is.

Yet there is no reason whatsoever why one could not take the energy as a function of the elastic strain alone, $w=w(u_{ij})$, and the stress as $\sigma_{ij}=-\partial w/\partial u_{ij}$, because rolling and slippage obviously cannot give rise to energy storage and maintain static stresses. Doing so offers a mechanical solution to the plastic impasse, because given an appropriate expression for the granular elastic energy w, we can use the associated stress, $\sigma_{ij}=\sigma_{ij}(u_{k\ell})$, as an elastic-strain–stress relation, for closing the force balance, $\nabla_j\sigma_{ij}=0$. This implies we can determine granular stress distributions just as systematically we do in elastic media. This approach, christened *granular elasticity* (GE), was introduced in Ref. [9] and explained in detail in the preceding paper [3]. Here, we employ it to calculate the stress distribution in silos and under point loads.

II. SILOS

A. Preliminaries

Calculation of granular stress is notoriously difficult, because the force balance,

$$\nabla_j\sigma_{ij}=\rho G_i \tag{1}$$

(where σ_{ij} is the symmetric stress tensor, ρ the density, and G_i the gravitational constant), a vector equation, is insufficient for determining all independent components of σ_{ij}. And there is no commonly accepted closure condition for granular systems, such as provided by elasticity for elastic media.

For tall silos, the classic approach is given by Janssen [1] who starts from the assumption that the ratio between the horizontal and vertical stress is constant,

$$k_J=\sigma_{rr}/\sigma_{zz}. \tag{2}$$

(Though merely a matter of historic interests, one may note that the original Janssen model considered only the average stress over a horizontal slice, see Ref. [2].) For a two-dimensional silos this closure condition suffices to close Eq. (1) and fully determine the three components $\sigma_{xx},\sigma_{xy},\sigma_{yy}$. For a cylindrical (or other three-dimensional) silo, this is not enough. Assuming in addition that σ_{zz} only depends on z, not on r, Janssen finds the vertical stress σ_{zz} saturating exponentially with height—a result well verified by observation—but leaves σ_{rz} and all three radial components, components $\sigma_{\theta\theta}$, $\sigma_{r\theta}$, and $\sigma_{z\theta}$ undetermined.

Having calculated σ_{zz}, one needs the value of k_J to obtain σ_{rr}, usually provided by

$$k_J\simeq 1-\sin\varphi, \tag{3}$$

where φ denotes the yield angle measured in triaxial tests. This makes φ the only bulk material parameter in silo stress distributions. We shall refer to this as the Jaky formula, although it is also attributed to Kézdi. Being important for the structural stability of silos, this formula is (with a safety factor of 1.2) part of the construction industry standard, see e.g., DIN 1055-6, 1987. We believe this formula goes well beyond its practical relevance, and that it is a key to understanding granular stresses, because it demonstrates the intimate connection between stress distribution and yield, a connection that has not gained the wide attention it deserves. Within the framework of linear elasticity, in which the stress will depend on the elastic coefficients, but not the yield angle, this connection is quite obscure.

Granular elasticity as presented in Ref. [3] provides an elastic-strain–stress relation for closing Eq. (1). Here, we aim to validate it for the silo geometry. Calculating all six components of the stress tensor, σ_{ij}, for a tall silo, we find both Janssen assumptions satisfied to within 1%, and the Janssen constant k_J well rendered by the Jaky formula. We take the agreement on these important features to be a support of granular elasticity.

In addition to these classic results, there has been many recent experimental activities in connection to granular stress, some of which performed in silos [4,5]. (And there was a satisfactory attempt of using linear elasticity to account for the normal stress at the silo bottom [6].) Although these experimental results, mainly on preparation dependence of the stress and the so-called overshoot, are intriguing, we reserve a comparison to future works, because of three reasons. The first is, the purpose of this paper is a qualitative validation for granular elasticity. It is sensible to first establish granular elasticity as sound and legitimate, before employing the theory (or a fine-tuned version of it) to account for the many features observed at present.

The second reason concerns preparation dependence itself: As discussed in Ref. [3], it is not clear how to include "fabric anisotropy" macroscopically, and whether any of it remains after shear-induced anisotropy is properly accounted for. So the only obvious and clearly defined quantity that will explain preparation dependence is a nonuniform density frozen in at preparation. Yet to calculate its influence, we need the measured density field of a given preparation as input. This, unfortunately, is as yet not available (though one might of course make an educated guess as in the case of sand piles). The third reason concerns overshoot, the surprising phenomenon that putting a weight that exerts the saturation pressure σ_{zz}^{∞} on top of the bulk goods in a silo, the vertical stress σ_{zz} responds by first deviating from σ_{zz}^{∞} (or "overshooting,") before returning to it further down. We believe overshoot tells us a lot about granular boundary conditions, but less about granular bulk behavior: Overshoot is clearly contingent on specially chosen boundary conditions, because it vanishes if we duplicate the stress distribution from lower down, where the pressure is saturated, and use it as the boundary conditions for the top. Yet at the moment, our aim is to validate a new set of differential equations for the bulk employing conventional boundary conditions.

By combining isotropic linear elasticity and Rowe's model of dilatancy [7], Evesque has also derived the Jaky formula [8], though the physics and the connection to our result remain opaque: Noting linear elasticity gives $k_J = \nu/(1-\nu)$ and $\Delta/u_{zz}=2\nu-1$ (with ν denoting the Poisson ratio and $\Delta \equiv -u_{\ell\ell}$), or equivalently $\Delta/u_{zz}=(k_J-1)/(k_J+1)$, Evesque boldly identifies Δ/u_{zz} as dilatancy (although dilatancy is known to vanish in linear elasticity). He then relates k_J to φ by equating this dilatancy to that from Rowe's micromechanical model, $\partial\Delta/\partial u_{zz}=k_J^{-1}\cot^2(\pi/4+\varphi/2)-1$.

Next, we summarize granular elasticity, see Ref. [3] for details, derivation, and a careful explanation why we believe it is appropriate for static granular stresses. It consists mainly of a relation between elastic-strain $u_{k\ell}$ and the stress σ_{ij}, given as

$$\sigma_{ij} = K\Delta\,\delta_{ij} - 2\mu u_{ij}^0, \tag{4}$$

where

$$K \equiv \mathcal{B}\sqrt{\Delta}\left(1+\tfrac{1}{2}u_s^2/\Delta^2\xi\right), \quad \mu \equiv \sqrt{\Delta}\mathcal{B}/\xi, \tag{5}$$

and $\Delta \equiv -u_{\ell\ell}$, $u_s^2 \equiv u_{ij}^0 u_{ij}^0$, $u_{ij}^0 \equiv u_{ij} - \frac{1}{3}u_{\ell\ell}\delta_{ij}$. This relation contains two coefficients, $\mathcal{B}$ and ξ. The first is a function of the void ratio e, and a measure of the total stiffness. The second is related to the Coulomb yield. If the shear σ_s goes beyond

$$\sigma_s = P\sqrt{2/\xi} \tag{6}$$

(where $P \equiv \frac{1}{3}\sigma_{\ell\ell}$, $\sigma_s \equiv \sqrt{\sigma_{ij}^0\sigma_{ij}^0}$, $\sigma_{ij}^0 \equiv \sigma_{ij} - P\delta_{ij}$), no static, elastic solution is possible, because an eigenvalue of the stiffness tensor $M_{ijk\ell} \equiv \partial\sigma_{ij}/\partial u_{k\ell}$, written as a 6×6 matrix, turns negative. In a triaxial geometry, taking the vertical stress as $\sigma_3 = p+q$, the lateral stress as $\sigma_1 = p$, and the Coulomb angle as $\sin\varphi \equiv (\sigma_3-\sigma_1)/(\sigma_3+\sigma_1) = q/(2p+q)$, the yield condition Eq. (6) leads directly to

$$\sin\varphi = 3/(2\sqrt{3\xi}+1), \tag{7}$$

see Ref. [9]. As in all our works, we take ξ as 5/3, associated with a triaxial yield angle of 33° [10].

Note that u_{ij} is the elastic strain field, which is a small fraction of the total strain and the part that contributes reversibly to the energy w, see the detailed discussion in the accompanying paper [3]. Although Eq. (4) is nonlinear, all terms are $\sim u_{ij}^{1.5}$, and should be taken as the lowest order approximation—which is appropriate since elastic deformations are typically tiny, rarely exceeding 10^{-4}. For the same reason, we may take $u_{ij} = \frac{1}{2}(\nabla_i U_j + \nabla_j U_i)$, with U_i the elastic displacement, and neglect the higher order terms $\sim(\nabla U)^2$.

For uniform void ratio, $\mathcal{B}$ is constant and a scale factor, and as such does not alter the stress, only the elastic strain, see, Ref. [3]. Employing Eq. (4) to calculate granular stress, the only material parameter is therefore quite generally the yield angle φ. In the following, we shall first numerically calculate the stress in a tall cylindrical silo using granular elasticity, assuming uniform void ratio and taking $\xi = 5/3$. After verifying that $k_J = \sigma_{rr}/\sigma_{zz}$ is indeed a spatial constant, we assume next that it holds for any value of ξ to validate the Jaky formula.

B. Finite element calculation of the stress in silos

Next, we embark on solving the boundary value problem given by the force balance, $\nabla_j\sigma_{ij} = \rho G_i$, and the stress-strain relation Eqs. (4) and (5), in an axially symmetric silo of radius R and height H ($\gg R$), employing the commercial finite-element software of FEMLAB. In cylindrical coordinates, with $\lambda \equiv K - 2\mu/3$ as the Lamé coefficient, and the gravity $G = G_z > 0$ along z, these equations are

$$\partial_r\sigma_{rr} + \partial_z\sigma_{rz} + (\sigma_{rr}-\sigma_{\theta\theta})/r = 0, \tag{8}$$

$$\partial_r\sigma_{rz} + \partial_z\sigma_{zz} + \sigma_{rz}/r - \rho G = 0, \tag{9}$$

$$\sigma_{rr} = \lambda\Delta - 2\mu\partial_r U_r, \quad \sigma_{zz} = \lambda\Delta - 2\mu\partial_z U_z, \tag{10}$$

$$\sigma_{rz} = -\mu(\partial_r U_z + \partial_z U_r), \quad \sigma_{\theta\theta} = \lambda\Delta - 2\mu U_r/r, \tag{11}$$

$$\Delta = -(U_r/r + \partial_r U_r + \partial_z U_z), \tag{12}$$

$$u_s^2 = (U_r/r)^2 - \tfrac{1}{3}\Delta^2 + (\partial_r U_r)^2 + (\partial_z U_z)^2 + \tfrac{1}{2}(\partial_z U_r + \partial_r U_z)^2. \tag{13}$$

As mentioned above, the Janssen model starts from two assumptions: $k_J \equiv \sigma_{rr}/\sigma_{zz}$ is a constant; and σ_{zz} depends only on z, not on r, implying the same for σ_{rr}. (Amontons law is usually listed as a third assumption.) Our numerical results not only confirm the Janssen outcome of saturating pressure, they show that both starting points are well satisfied. This is important, because given the starting points, it is simple algebra to obtain the results: Multiplying Eq. (9) with r and integrating the result over dr, from 0 to R, leads to $R\partial\sigma_{zz}/\partial z - \rho GR + 2\sigma_{rz}|_{r=R} = 0$, in which the last term may be substituted with $2\mu_f\sigma_{rr} = 2\mu_f k_J \sigma_{zz}$. The solution is $\sigma_{zz} = \sigma_{zz}^{\rm sat} - (\sigma_{zz}^{\rm sat} - P_0)\exp(-\rho Gz/\sigma_{zz}^{\rm sat})$, where $P_0 = \sigma_{zz}(z=0)$ is the applied pressure at the silo top, while $\sigma_{zz}^{\rm sat} \equiv \rho GR/2\mu_f k_J > 0$ is the vertical stress at large depths ($z \gg \sigma_{zz}^{\rm sat}/\rho G = R/2\mu_f k_J$).

Our boundary conditions are (1) a nearly free surface at the top, $\sigma_{rz}=0$, $\sigma_{zz}=P_0 \sim 0$. (As $\Delta=0$ is a singular point of the present theory, a load P_0 is added at the top to avoid numerical problems. Being around 5% of $\sigma_{zz}^{\rm sat}$, it should be too small to alter any essential features of our results.) (2) Amontons law along the side wall: $\sigma_{rz} = \mu_f \sigma_{rr}$ for $r=R$, with $\mu_f > 0$; an infinitely rigid container, $U_r = 0$. (The last condition only asserts that the elastic part of the displacement vanishes, not the plastic one.) (3) Glued granular material at the bottom, $U_r, U_z = 0$ (assumed for simplicity). Finally, for $r=0$, we have $\sigma_{rz}=0$, $U_r=0$ because of axial symmetry, and $\sigma_{rr} = \sigma_{\theta\theta}$ to render Eq. (8) regular.

Figure 1 shows the results computed using $\xi = 5/3$ and $\mu_f = 0.2$. Within the numerical accuracy, no difference is found between the calculated σ_{zz} and the Janssen profile—except near the bottom, where the influence of the boundary condition is felt. Both the off-diagonal component σ_{rz} and $\sigma_{\theta\theta}$, not accessible within the Janssen model, are calculated. σ_{rz} is displayed in Fig. 1, $\sigma_{\theta\theta}$ is almost equal to σ_{rr}. Similar results are found for other values of ξ and μ_f, always showing that the two Janssen assumptions are well satisfied: The spatial variation of the computed k_J stays within 1%, even in the transient regions near the top and bottom; also, the radial variation of σ_{zz} is tiny, see inset of Fig. 1.

C. Verification of the Jaky formula

In the above example, we find $k_J \approx 0.4$ and $\sigma_{zz}^{\rm sat}/\rho GR \approx 6$ for $\xi = 5/3$ and $\mu_f = 0.2$. Next, we let both ξ, μ_f vary, in order to find the functional dependence of $k_J(\xi, \mu_f)$. For this purpose, as k_J has been shown to be a spatial constant, it is permissible to go to the saturated limit, in which all stress and strain components are independent of z. Then Eq. (9) may be integrated to yield $\sigma_{zr} = \frac{1}{2}\rho Gr$. Also, the displacement $U_r = U_r(r)$ must not depend on z, see the second of Eq. (11). Inserting these into the first of Eq. (11), we have $\mu\partial_r U_z = -\frac{1}{2}\rho Gr$, or $U_z - cz = -\frac{1}{2}\int \rho Gr/\mu dr = -\int \rho Gr/(A\sqrt{\Delta})dr$, where c is an integration constant. (Note $\sqrt{\Delta}$ is r dependent.) Inserting these into Eq. (8) and denoting ∂_r as $'$, we have

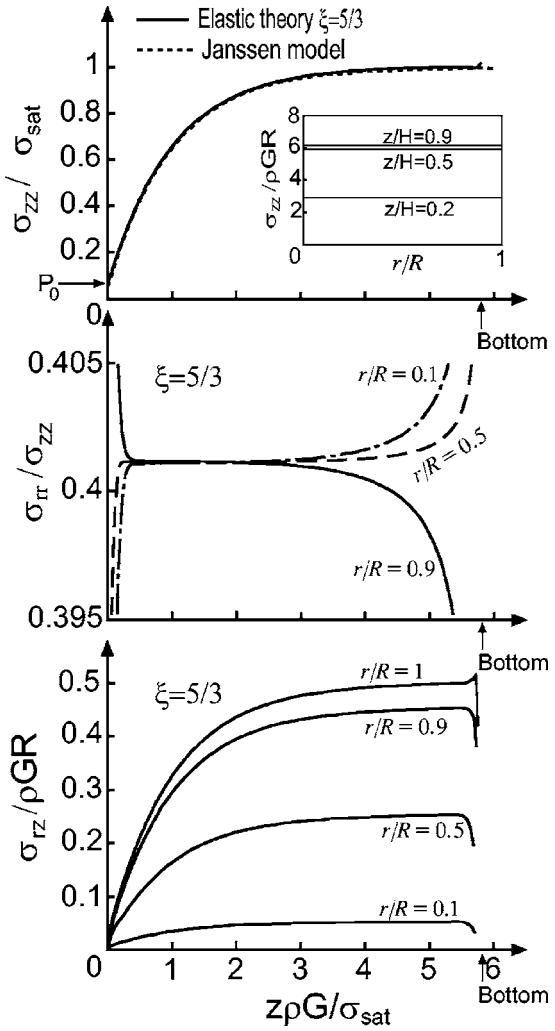

FIG. 1. Stress components calculated using Eq. (3) and the force balance. The upper figure shows the vertical stress σ_{zz}; the middle figure shows Janssen's ratio, $k_J = \sigma_{rr}/\sigma_{zz}$ (note the amplified vertical scale); and the lowest figure gives σ_{rz} at different radii—all as functions of the depth z.

$$r(\lambda\Delta - 2\mu U_r')' = 2\mu(U_r' - U_r/r), \tag{14}$$

where $\lambda \equiv K - \frac{2}{3}\mu$ and μ are given by Eq. (5), with $-\Delta = U_r/r + U_r' + c$ and $u_s^2 = U_r^2/r^2 - \frac{1}{3}\Delta^2 + (U_r')^2 + c^2 + \frac{1}{2}(\rho Gr/A\sqrt{\Delta})^2$. Equation (14) is an ordinary differential equation for $U_r(r)$, which we have solved numerically employing the boundary conditions $U_r \sim r$ for $r \to 0$, and $U_r = 0$ at $r = R$. From U_r, the saturated stresses $\sigma_{zz}, \sigma_{rr}, \sigma_{\theta\theta}$ can be computed, yielding k_J and μ_f (effectively relating c to μ_f; while the second constant $\rho G/A$ cancels). In agreement with our finite-element calculation, $k_J \equiv \sigma_{rr}/\sigma_{zz}$ hardly varies with r. So we may regard k_J as a material-dependent constant, given by ξ, μ_f. We find k_J almost unrelated to μ_f, but strongly increases with ξ, see Fig. 2(a). As granular materials only support limited shear forces, $\mu_f = \sigma_{rz}/\sigma_{rr}|_{r=R}$ cannot exceed a maximal value. This is indeed what we find: Solutions of Eq. (14) are real only when μ_f is within the boundary given by the thick curve of Fig. 2(a). [This curve may also be obtained from Eq. (6) noting $\sigma_{rr} \simeq \sigma_{\theta\theta}$.]

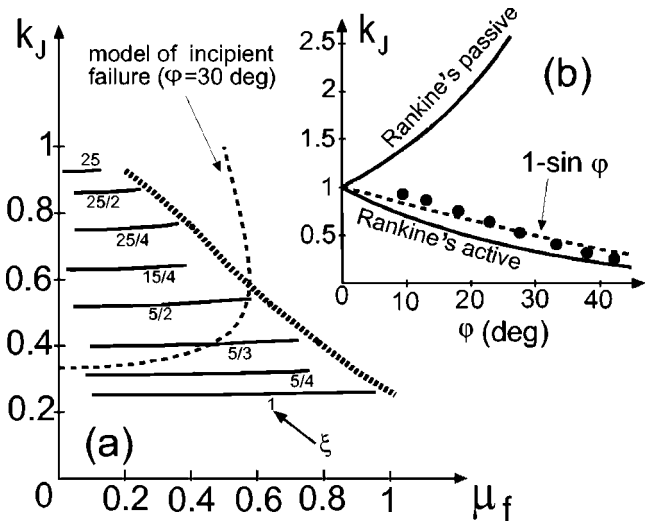

FIG. 2. (a) The Janssen ratio k_J increases only slightly with the wall friction μ_f at constant ξ, and ends at the boundary (thick curve) determined by the yield condition. The dotted line is given by the IF model, with $\varphi=30°$. (b) Variation of k_J with the yield angle φ, given, respectively, by the Rankine states (solid lines), the Jaky formula (dotted line), and the present theory (circles).

Neglecting the off-diagonal stress σ_{hv} and taking the Coulomb condition as $|(\sigma_h-\sigma_v)/(\sigma_h+\sigma_v)|\leqslant \sin\varphi$, or equivalently

$$\tan^2\left(\frac{\pi}{4}-\frac{\varphi}{2}\right)\leqslant \sigma_h/\sigma_v \leqslant \tan^2\left(\frac{\pi}{4}+\frac{\varphi}{2}\right),$$

the Rankine states are given by the lower and the upper limits of this equation, see Ref. [11]. The two curves designated as Rankine's in Fig. 2(b) are obtained by taking in addition $\sigma_{rr}=\sigma_h$ and $\sigma_{zz}=\sigma_v$. Including σ_{rz}, the Coulomb condition (in cylindrical coordinates and approximating $\sigma_{rr}\simeq\sigma_{\theta\theta}$) is

$$[(\sigma_{rr}-\sigma_{zz})^2+4\sigma_{rz}^2]/(\sigma_{rr}+\sigma_{zz})^2\leqslant \sin^2\varphi,$$

which is more confining than the Rankine limits. So k_J must in fact always lie between both limits, irrespective of σ_{rz}. The IF model (again with $\sigma_{rr}\simeq\sigma_{\theta\theta}$) assumes $(\sigma_{rr}-\sigma_{zz})^2+4\sigma_{rz}^2=(\sigma_{rr}+\sigma_{zz})^2\sin^2\varphi$. In the saturation region of the silo (where $\partial_z=0$), we have $\sigma_{rz}=\rho Gr/2$, $\sigma_{rr}=\text{const}=\rho GR/(2\mu_f)$, yielding a dependence in this model of k_J with μ_f,

$$(1-k_J^{-1})^2+(2\mu_f r/R)^2=(1+k_J^{-1})^2\sin^2\varphi.$$

This is depicted by the dashed line in Fig. 2(a). (Note that this k_J is indeed between the two Rankine values, being 1/3 and 3 for $\varphi=30°$.) In practice, k_J is found to be given by the Jaky formula, $k_J=1-\sin\varphi$. As Eq. (7) relates φ for triaxial tests with ξ, we can easily convert $k_J(\xi)$ of Fig. 2(a) to $k_J(\varphi)$, as shown in Fig. 2(b). The agreement is obvious.

III. POINT LOADS

A. Introduction

The pressure distribution at the bottom of a layer of sand exposed to a localized load at its top (the so-called Greens function of stress propagation) was carefully studied recently [5,12–14]. The normal force distribution (or pressure) was measured at the bottom of the layer, and a single peak was found [15]. In Ref. [5], the samples were prepared by rainlike pouring of grains, presumably resulting in a homogeneous density, and the peak is found narrower by about 10% than predicted by isotropic linear elasticity. In Ref. [12], this experiment was performed using samples that were prepared somewhat more intrusively, either by pressing with a plate after a thin layer of sand is added, and repeating the procedure until the desired height is achieved, or by pulling a sieve up from the bottom of the sand. At least the first method is expected to result in some density inhomogeneities. Numerical simulations of this experiment were reported in Ref. [13], in which the point load is allowed to have two different inclinations, normal and tilted by 45°. Agreement was found comparing these results to discrete-element calculation of isotropic linear elasticity (ILE) with adjustable elastic coefficients. In Ref. [14], Atman *et al.* performed the same experiment on a sheared slab of sand, and on one containing avalanche-compacted layers. Taking the shear and avalanches as breaking the isotropy of the granular texture [16], and viewing the point load as a tool probing this fact, the authors postulated elastic coefficients appropriate for the anisotropy, and employed these to calculate the stress, again finding agreement.

In this section, we employ some of these results to validate granular elasticity as presented in Ref. [3]. Since a point load on top of a layer is one of three typical granular geometries (the other two are silos and sand piles), it is important to verify that granular elasticity properly accounts for its stress distribution. As discussed in Ref. [3], the calculation employing granular elasticity is carried out without any fit parameters—as in all our works, we take $\xi=5/3$, while $\mathcal{B}_0$ does not enter the stress expression. Hence even qualitative agreement with experimental data would be accepted as validation. Yet, as we shall see, the results from granular elasticity compare quite favorably with isotropic and anisotropic linear elasticity, are just as good or better.

In choosing experimental results to compare granular elasticity with, we select those where a uniform density may be plausibly assumed, because nonuniform densities influence the stress distribution, and we need the measured density field (not usually known) to calculate its contribution. More specifically, we shall consider (i) the experiment using samples prepared by rainlike pouring of grains [5], (ii) the numerical simulation of normal and oblique top forces [13], and (iii) the sheared slab of Ref. [14]. Although the other experiments are left out here, we believe our selection suffices to show that granular elasticity is an appropriate framework for describing and understanding static granular stress distributions, far superior to linear elasticity. Also, we hope that this comparison provides an incentive for measuring the density field at the same time with granular stresses.

B. The FEMLAB calculation

1. The differential equations

We consider a layer of sand, of thickness h, in a cylindrical container, with a load force on the piston at the center,

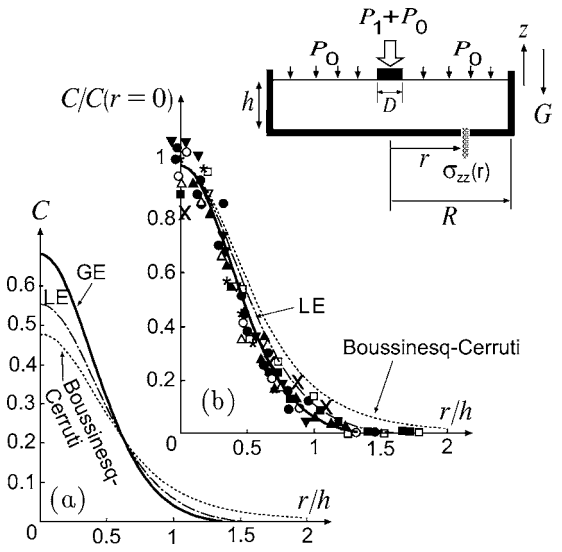

FIG. 3. (a) Bold line shows the normal stress C at the bottom calculated from granular elasticity assuming glued grains at the bottom. "LE" stands for the same calculation, though employing isotropic linear elasticity, and "Boussinesq-Cerruti" for the analytic solution of an infinite half-space of a linearly elastic body. (b) The same three curves renormalized by their values at $r=0$; symbols are the measured data of Ref. [5]. Inset shows the geometry.

see the inset of Fig. 3(b). The container diameter $2R$ is much larger than the piston diameter D, so the influence of side walls on the bottom pressure $\sigma_{zz}(r)$ should be negligible, and the computed pressure may be directly compared to the measurements, done in a rectangular vessel [5]. In the cylindrical coordinates the force balance (1) and Hooke's law (4) are

$$\partial_r\sigma_{rr} + \partial_z\sigma_{rz} + (\sigma_{rr} - \sigma_{\theta\theta})/r = 0, \tag{15}$$

$$\partial_r\sigma_{rz} + \partial_z\sigma_{zz} + \sigma_{rz}/r + \rho G = 0, \tag{16}$$

$$\sigma_{rr} = \lambda\Delta - 2\mu\partial_r U_r, \quad \sigma_{zz} = \lambda\Delta - 2\mu\partial_z U_z, \tag{17}$$

$$\sigma_{rz} = -\mu(\partial_z U_r + \partial_r U_z), \quad \sigma_{\theta\theta} = \lambda\Delta - 2\mu U_r/r, \tag{18}$$

where $\lambda \equiv K - 2\mu/3$ denotes the Lamé coefficient (also strain dependent), and U_r, U_z are the horizontal and vertical displacement, respectively. We choose the gravity along the $-z$ direction, so that $G=-G_z>0$. The volumeric and shear strain are

$$\Delta = -U_r/r - \partial_r U_r - \partial_z U_z \tag{19}$$

$$u_s^2 = (U_r/r)^2 - \Delta^2/3 + (\partial_r U_r)^2 + (\partial_z U_z)^2 + (\partial_z U_r + \partial_r U_z)^2/2. \tag{20}$$

As written, Eqs. (15)–(20) are the same as those of isotropic linear elasticity (ILE), with the only exception that the elastic moduli K, μ are strain dependent, given by inserting Eqs. (19) and (20) into (5). These equations are solved for U_r, U_z employing the boundary conditions: (i) $U_z=0$, $U_r=0$ at the bottom, implying an infinitely rigid bottom, with the grains glued; or $U_z=0$, $\sigma_{rz}=0$, assuming that the grains may slide sideways without any friction. (No significant differences were found.) (ii) $U_r=0$ and $\sigma_{rz}=0$ at the side walls $r=R$. (We assume for simplicity that the side walls are rigid and frictionless, since they are too far from the piston to be relevant.) (iii) At the top surface, $\sigma_{zz}=P_1+P_0$ under the piston and $\sigma_{zz}=P_0$ elsewhere, $\sigma_{rz}=0$ everywhere.

The uniform background pressure $P_0(\ll P_1)$ at the top is added to ensure that the sand is sufficiently compressed and that $\Delta>0$ everywhere. (Note P_0 may also be interpreted as an internal cohesion pressure.) Without P_0, the linearly elastic solution contains a region where Δ is negative, unphysical for cohesionless materials. In granular elasticity, Δ cannot be negative, because $\Delta=0$ is a singular point, at which the system becomes unstable. In reality, we expect the sand to pile up slightly as a ring around the piston, the weight of which stabilizes the system below. A P_0 much smaller than P_1 should not change the stress distribution significantly, but enables us to avoid having to consider this ring explicitly.

Of the six parameters in the equations, $G, D, P_0, \mathcal{B}, P_1, h$, we may (for $\mathcal{B}$=constant) eliminate three by making all variables dimensionless. Taking the coordinates as $\tilde{r}=r/h$, $\tilde{z}=z/h$, the displacements as $\tilde{U}_r=(\mathcal{B}/P_1)^{2/3}U_r/h$, $\tilde{U}_z=(\mathcal{B}/P_1)^{2/3}U_z/h$, the stress as $\tilde{\sigma}_{ij}=\sigma_{ij}/P_1$, the piston diameter as $\tilde{D}=D/h$, the gravity constant as $\tilde{G}=\rho h G/P_1$, and the background pressure as $\tilde{P}_0=P_0/P_1$, the equations for these dimensionless quantities are

$$(\partial\tilde{\sigma}_{rr}/\partial\tilde{r}) + (\partial\tilde{\sigma}_{rz}/\partial\tilde{z}) + (\tilde{\sigma}_{rr} - \tilde{\sigma}_{\theta\theta})/\tilde{r} = 0, \tag{21}$$

$$(\partial\tilde{\sigma}_{rz}/\partial\tilde{r}) + (\partial\tilde{\sigma}_{zz}/\partial\tilde{z}) + \tilde{\sigma}_{rz}/\tilde{r} + \tilde{G} = 0 \tag{22}$$

with

$$\tilde{\sigma}_{rr} = \tilde{\lambda}\tilde{\Delta} - 2\tilde{\mu}\frac{\partial\tilde{U}_r}{\partial\tilde{r}}, \quad \tilde{\sigma}_{zz} = \tilde{\lambda}\tilde{\Delta} - 2\tilde{\mu}\frac{\partial\tilde{U}_z}{\partial\tilde{z}}, \tag{23}$$

$$\tilde{\sigma}_{rz} = -\tilde{\mu}\left(\frac{\partial\tilde{U}_r}{\partial\tilde{z}} + \frac{\partial\tilde{U}_z}{\partial\tilde{r}}\right), \quad \tilde{\sigma}_{\theta\theta} = \tilde{\lambda}\tilde{\Delta} - 2\tilde{\mu}\frac{\tilde{U}_r}{\tilde{r}} \tag{24}$$

and

$$\tilde{\mu} = \tfrac{3}{5}\tilde{\Delta}^{1/2}, \quad \tilde{K} = \tilde{\Delta}^{1/2}\left(1 + \tfrac{3}{10}\tilde{u}_s^2/\tilde{\Delta}^2\right), \tag{25}$$

$$\tilde{\Delta} = -\tilde{U}_r/\tilde{r} - (\partial\tilde{U}_r/\partial\tilde{r}) - (\partial\tilde{U}_z/\partial\tilde{z}), \tag{26}$$

$$\tilde{u}_s^2 = (\tilde{U}_r/\tilde{r})^2 - \tfrac{1}{3}\tilde{\Delta}^2 + (\partial\tilde{U}_r/\partial\tilde{r})^2 + (\partial\tilde{U}_z/\partial\tilde{z})^2 + \tfrac{1}{2}(\partial\tilde{U}_r/\partial\tilde{z} + \partial\tilde{U}_z/\partial\tilde{r})^2, \tag{27}$$

where $\tilde{\mu}=(\mathcal{B}/P_1)^{1/3}\mu/\mathcal{B}$, $\tilde{\lambda}=(\mathcal{B}/P_1)^{1/3}\lambda/\mathcal{B}$, $\tilde{\lambda}\equiv\tilde{K}-2\tilde{\mu}/3$, $\tilde{\Delta}=(\mathcal{B}/P_1)^{2/3}\Delta$, $\tilde{u}_s=(\mathcal{B}/P_1)^{2/3}u_s$. The boundary conditions at the top surface are $\tilde{\sigma}_{zz}=1+\tilde{P}_0$ under the piston, $\tilde{\sigma}_{zz}=\tilde{P}_0$ elsewhere, and $\tilde{\sigma}_{rz}=0$ everywhere. At the bottom we have $\tilde{U}_z=0$, and $\tilde{U}_r=0$ for the glued case, $\tilde{\sigma}_{rz}=0$ for the gliding case. For the side wall we have $\tilde{U}_r=0$ and $\tilde{\sigma}_{rz}=0$. Note that the rescaled stress profile $\tilde{\sigma}_{zz}(\tilde{r},\tilde{z})$ depends only on three parameters: $\tilde{G}, \tilde{D}, \tilde{P}_0$.

The quantity being compared between theory and experiment [5] is essentially the zz component of the stress at the bottom, $z=h$ or $\tilde{z}=1$, from which the weight and the background pressure P_0 (zero in the experiment) is subtracted; the result is rescaled by the force on the piston, $F=P_1\pi D^2/4$, and multiplied by the layer depth squared h^2,

$$C = (h^2/F)(\sigma_{zz}^{\text{Bottom}} - P_0 - \rho hG) = (4/\pi\tilde{D}^2)(\tilde{\sigma}_{zz}^{\text{Bottom}} - \tilde{P}_0 - \tilde{G}). \tag{28}$$

Because $2\pi\int_0^R \sigma_{zz}^{\text{Bottom}} r dr = F + 2\pi\int_0^R (P_0+\rho hG) r dr$, we have the normalization condition

$$2\pi\int_0^R C\tilde{r}d\tilde{r} = 1. \tag{29}$$

The profile $C(\tilde{r})$ depends by up to 5% on $\tilde{G}$, and by up to 3% on $\tilde{D}$, $\tilde{P}_0$ and the choice between glued and sliding boundary condition at the bottom. If we neglect these, we may take $C(\tilde{r})$ as an approximately universal function. This agrees with the fact that data obtained from samples of different thickness h collapse onto the same curve [5].

Equations (21) and (22) are two partial differential equations, which are solved numerically for $\tilde{U}_r(\tilde{r},\tilde{z})$ and $\tilde{U}_z(\tilde{r},\tilde{z})$ using a finite-element code built into the commercial software of FEMLAB. Two cases have been studied: (i) the localized force is applied vertically on top of the surface, and the results are compared with the measurements reported in Ref. [5]; (ii) the force is inclined by 45°, and the results are compared to the simulation of Ref. [13].

2. Results: Piston with vertical force

In the calculation $\tilde{P}_0 \sim 0.3$, $\tilde{D} \sim 0.182$ are used, with the container box having a diameter of $32D$, large enough to render the influence of side walls insignificant. A great number of grid cells (50 000–150 000 cells) are considered, concentrated mainly at the center, in particular below the piston, as well as at the bottom. The calculated stress profile C is a single peak curve centered at the position of the localized piston force. The full-line curve of Fig 3(a) shows the result for granular elasticity (taking $\tilde{G}=4.13$, which for the bulk density of $\rho_g = 2660\ \text{kg/m}^3$ approximately renders the experimental circumstances: a height of 80 mm with a piston pressure of 500 Pa). The dashed line give the result from ILE, employing the same boundary conditions, while the dotted line displays the analytical solution by Boussinesq and Cerruti of an infinite half-space of a linearly elastic body [18]. The ILE result is narrower than the analytic one [12], but the narrowest line is from granular elasticity, which shows near perfect agreement with the experiment, see especially Fig. 3(b), where the curves are rescaled by their values at $r=0$.

In the experimental setup, the force on the top has a finite extension, with $D \sim 11$ mm and $h \sim 30$–100 mm, or $\tilde{D}$ varying between 0.1 and 0.4. In this range, no noticeable variation of C is found in our calculation. With respect to the other two parameters, $\tilde{P}_0$ and $\tilde{G}$, one needs to realize that although both drop out for LE, due to linear superposition and Eq. (28), circumstances are less clear for granular elasticity. However, we checked the asymptotics and did not find any significant effects due to the finiteness of $\tilde{P}_0$, ensuring that the calculation agrees with experiment, in which the layer top off the piston is a free surface, $\tilde{P}_0 \to 0$. On the other hand, a slight increase of the peak half width is observed as $\tilde{G}$ goes to zero, see Fig. 4. Taking $\rho G \sim 16$ Pa/mm (typical for sand), $P_1 = 500$ Pa and $h \sim 30$–100 mm, we have $\tilde{G}$ varying between 1 and 3.2, a range in which the rescaled half-width W/h of granular elasticity is found around 0.95, close enough to the measured 0.94. (The values for ILE and Boussinesq-Cerruti are 1.04 and $2\sqrt{2^{2/5}-1} \approx 1.13$, respectively.) Clearly, the inclusion of gravity is essential for the agreement between granular elasticity and experiment. Finally, C also changes with the boundary conditions at the bottom, with the half-width somewhat broader (and the maximum correspondingly lower) for the glued condition, see Fig. 4. A similar behavior is found for ILE.)

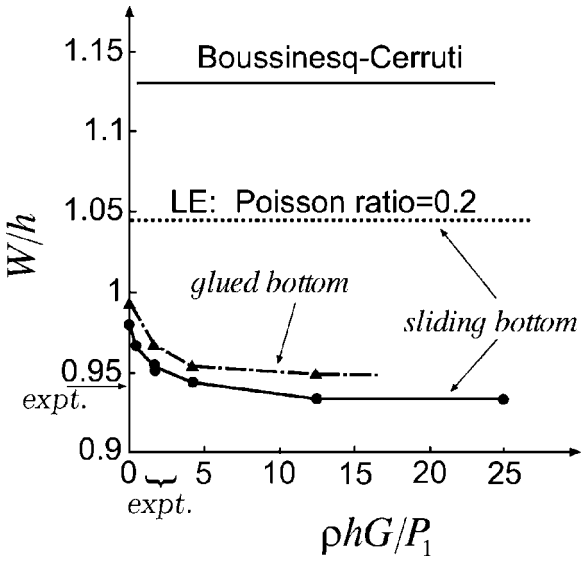

FIG. 4. Symbols: Variations of the half-width with the rescaled gravity constant for the two boundary conditions discussed in the text, as computed using granular elasticity. The experimental half-width of 0.94 was measured for $\tilde{G} \equiv \rho hG/P_1$ varying between 1 and 3.2, as indicated.

3. Results: Piston with inclined force

Changing the cylinder of the last section to a cylindrical ring, the stress distribution produced by an oblique load can be computed preserving the cylindrical symmetry, see the inset in the lower part of Fig 5. When the diameter of the ring is sufficiently large, the solutions approach those of a two-dimensional solution, but the same code implementation can be used to produce the simulations. [Different ratios were tried, most calculations were done with a width of 0.36 m and a ring diameter of 10 m (ratio 0.036). There were no visible changes in the result for a ring diameter of 100 m.]

Figure 3 displays the stress components, σ_{zz} and σ_{rz}, as computed using granular elasticity (full lines), for vertical

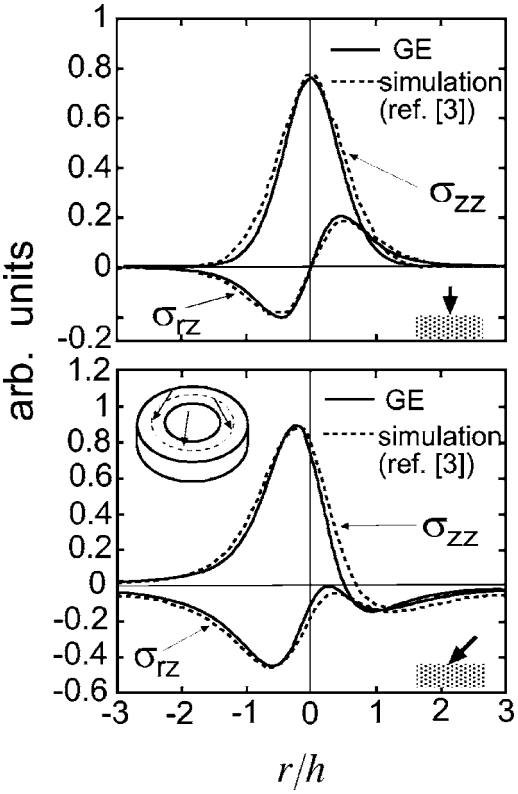

FIG. 5. Computed bottom pressure (full lines) for localized top force, either vertical (upper figure) or inclined by 45° (lower figure). The dashed lines are 2D simulation, as taken from Fig. 10 of Ref. [13], for rainlike pouring.

(upper figure) and oblique load (45°, lower figure). In the lower figure, the stress profiles are shifted from the center, and show essentially quantitative agreement with the simulation works in Ref. [13] (dotted lines).

Note that the width of the dashed lines peaks are slightly broader than the full lines, and broader than peaks calculated in the fully rotationally symmetric configuration with central peak. The second fact is easily understandable, since the simulations are done effectively in two dimensions, and it is known from ILE that the stress curves are broader in 2D. For instance, the peak width of Boussinesq-Cerruti's solution is $2\sqrt{2^{2/5}-1} \approx 1.13$ for 3D, and $2\sqrt{\sqrt{2}-1} \simeq 1.29$ for 2D, see Ref. [19]. The peaks from granular elasticity are slightly narrower than given by the 2D simulation. This may be a result of the fact that the elastic energy, Eq. (4), is only appropriate for 3D calculations [20]. Also, in 2D simulations there is no stress nor strain in the third coordinate direction, while we solve the 3D equations in a 2D geometry.

C. Point load on sheared sand

Measuring the stress response to a point load in a sheared layer of sand, Atman *et al.* [14] took the sheared sand as an anisotropic medium and employed anisotropic linear elasticity to calculate the system's response to the point load. More specifically, subjecting a slab of sand to a vertical, normal force P_0 and a tangential, horizontal force F_s (both uniform), they found it to possess preferred orientations, along the

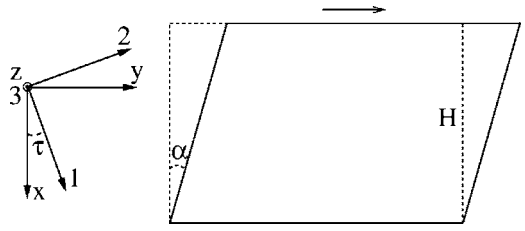

FIG. 6. Sketch of the 3D shear box. The stress σ_{ij} is diagonal in the coordinate system 1, 2, 3.

principle axes of compression and dilation, denoted, respectively, as 1 and 2, with 3 being the neutral direction, see Fig. 6. So Atman *et al.* postulated an anisotropic linear stress-strain relation in this frame, $\sigma_{ij}=K_{ijk\ell}u_{k\ell}$, and used it to calculate the stress response to a point load by solving the force balance,

$$\nabla_j \sigma_{ij} = K_{ijk\ell} \nabla_j u_{k\ell} = 0. \tag{30}$$

Presenting the stress-strain relation $\sigma_{ij}=K_{ijk\ell}u_{k\ell}$ as

$$\begin{pmatrix} u_{11} \\ u_{22} \\ u_{33} \end{pmatrix} = \begin{pmatrix} -1/E_1 & \nu_{12}/E_2 & \nu_{13}/E_3 \\ \nu_{21}/E_1 & -1/E_2 & \nu_{23}/E_3 \\ \nu_{31}/E_1 & \nu_{32}/E_2 & -1/E_3 \end{pmatrix} \begin{pmatrix} \sigma_{11} \\ \sigma_{22} \\ \sigma_{33} \end{pmatrix},$$

$$\begin{pmatrix} 2u_{23} \\ 2u_{13} \\ 2u_{12} \end{pmatrix} = \begin{pmatrix} -G_{23}^{-1} & 0 & 0 \\ 0 & -G_{13}^{-1} & 0 \\ 0 & 0 & -G_{12}^{-1} \end{pmatrix} \begin{pmatrix} \sigma_{23} \\ \sigma_{13} \\ \sigma_{12} \end{pmatrix}, \tag{31}$$

(where the 3-direction was amended by the authors) and denoting $t \equiv E_2/E_1$, $u \equiv E_2/G_{12}$, they found that only certain combinations of t,u falling onto a curve (the dashed line of Fig. 7) are consistent with the measured stress. (As discussed in Ref. [3], the surface force F_s that maintains the shear is a

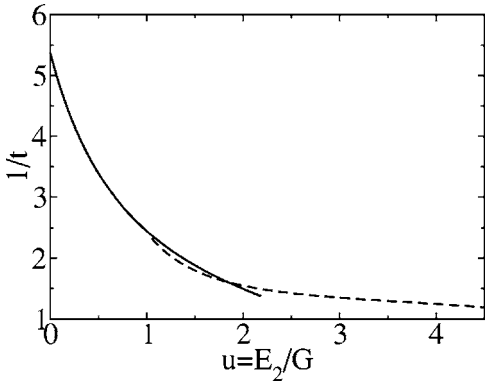

FIG. 7. $1/t \equiv E_1/E_2$ versus $u \equiv E_2/G_{12}$, as calculated employing granular elasticity (solid line), and as found by Atman *et al.*, Fig. 7 from Ref. [14] (dashed line), for the 3D shear box. The dashed line represents all points of a linear anisotropic elastic theory compatible with the measured tilt angle of $\beta=8°$. The solid line takes F_s as a parameter, with which both u and t decrease monotonically. The lower right point of the solid line, $1/t=1.38, u=2.18$, corresponds to $F_s=0$, and the upper left-hand point, $1/t=5.31, u=0.1$ corresponds to yield, $F_s=F_s^{\max}$. Both lines intersect at $1/t=1.61$, $u=1.83$, which corresponds to $F_s=0.54\times F_s^{\max}$.

proper boundary condition. But the total shear angle α of Fig. 6 is not, because it is not easily related to elastic displacements.)

Next, we calculate the coefficients of Eq. (31) within the framework of granular elasticity, as presented briefly in the introduction, and in greater details in Ref. [3]. We start with the force balance $\nabla_j(\sigma_{ij}+\delta\sigma_{ij})=0$, where σ_{ij} is the stress of the sheared layer of sand, and $\delta\sigma_{ij}$ the stress increment from the point load. Because $\nabla_j\sigma_{ij}=0$ holds without the load, so does $\nabla_j\delta\sigma_{ij}=0$. And if the point load is small enough, we may take $\delta\sigma_{ij}=M_{ijk\ell}\delta u_{k\ell}$, where $M_{ijk\ell}\equiv\partial\sigma_{ij}/\partial u_{k\ell}$. Therefore, the equation,

$$\nabla_j\delta\sigma_{ij}=M_{ijk\ell}\nabla_j\delta u_{k\ell}=0, \tag{32}$$

(assuming that σ_{ij} is constant) is the one to solve for calculating the stress increment. Since its appearance is the same as Eq. (30), we may identify $M_{ijk\ell}$ with $K_{ijk\ell}$. The formulas for $M_{ijk\ell}$ and its inverse $\lambda_{ijk\ell}$ (in the principle system in which σ_{ij} is diagonal) are given in Eqs. (17)–(21) of Ref. [3]. Rewriting them in the format of Eq. (31), the coefficients may be read off as (see the second reference of Ref. [17])

$$G_{13}=G_{23}=G_{12}=\mu, \tag{33}$$

$$E_i=\frac{27\mu(\mathcal{A}^5\sigma_s^2-8\mu^6\mathcal{B})}{9\mathcal{A}^5\sigma_s^2-72\mu^6\mathcal{B}-\mathcal{A}s_i^2}, \tag{34}$$

$$\nu_{ij}=\frac{1}{2}\frac{9\mathcal{A}^5\sigma_s^2-72\mu^6\mathcal{B}+2\mathcal{A}s_is_j}{9\mathcal{A}^5\sigma_s^2-72\mu^6\mathcal{B}-\mathcal{A}s_j^2}, \tag{35}$$

with $s_i\equiv 3\mathcal{A}^2\sigma_i^0-4\mu^3$, $\sigma_i^0\equiv\sigma_i-P$ (σ_i denotes the eigenvalues of σ_{ij} and $P\equiv\sigma_{ii}$ the pressure). Written as stress dependent, the shear moduli μ of Eq. (5) is

$$\mu\equiv\mathcal{A}\{[1+\sqrt{1-(\mathcal{B}/2\mathcal{A})(\sigma_s^2/P^2)}]P/2\mathcal{B}\}^{1/3}. \tag{36}$$

To obtain these coefficients explicitly, we now calculate σ_{ij} for a sheared slab of sand, diagonalize it and insert the result into these expressions.

Taking x to point down, and y, z to point horizontally, we consider a layer of sand extending from $x=0$ to $x=-H$, and infinitely along y, z, see Fig. 6. We take z to be the neutral direction, $U_z\equiv 0$, and allow spatial dependence only along x, or $U_x=U_x(x)$, $U_y=U_y(x)$. Solving $\nabla_j\sigma_{ij}=0$ with the boundary conditions, $\sigma_{xx}=P_0$, $\sigma_{xy}=F_s$ at $x=-H$, and $U_x=U_y=0$ at $x=0$, the solution is

$$U_x=-\Delta x,\quad U_y=-F_sx/(\mathcal{A}\sqrt{\Delta}), \tag{37}$$

$$\Delta^{3/2}=(3P_0+q)/[2\mathcal{A}(3\xi+5)], \tag{38}$$

$$q=\sqrt{3}\sqrt{3P_0^2-(3\xi+5)F_s^2}. \tag{39}$$

Inserting these into Eq. (4), the stress tensor is

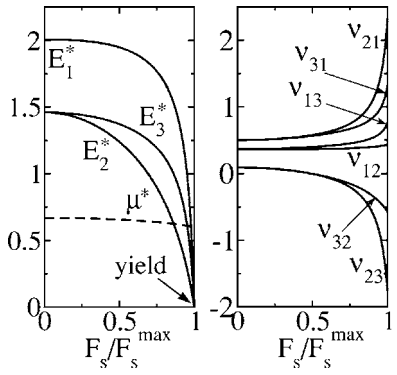

FIG. 8. The dimensionless Young moduli $E_i^\star$, $\mu^\star$ and the Poisson ratios ν_{ik} as functions of $F_s/F_s^{\max}$, where $E_i=E_i^\star\mathcal{A}(P_0/\mathcal{A})^{1/3}$ and $\mu=\mu^\star\mathcal{A}(P_0/\mathcal{A})^{1/3}$.

$$\sigma_{ij}=\begin{pmatrix}P_0 & F_s & 0\\ F_s & P_1 & 0\\ 0 & 0 & P_1\end{pmatrix}, \tag{40}$$

where $P_1\equiv[(3\xi+2)P_0-q]/(3\xi+5)$. The maximal possible value of F_s is found from the stability condition $u_s^2/\Delta^2\leqslant 2\xi$, or $F_s/P_0\leqslant\sqrt{\xi-\frac{1}{3}}/(\xi+\frac{2}{3})$.

In the experiment, we have $P_0=7.85$ kPa. Taking as usual $\xi=5/3$, the maximal force $F_s^{\max}$ is 3.88 kPa, and the maximal elastic shear angle, $\tan\alpha^{\rm ela}=F_s/(\mathcal{A}\sqrt{\Delta})$, is $\alpha_{\max}^{\rm ela}=0.0063°$. Clearly, we have $\alpha^{\rm ela}\ll\alpha$, where α, the total shear angle, is on the order of 10°, see Ref. [14].

In the principle system of diagonal stress, with the coordinates 1, 2, 3, the incremental stress-strain relation $\delta\sigma_{ij}=(\partial\sigma_{ij}/\partial u_{k\ell})\delta u_{k\ell}$ takes the form of Eq. (31), with the coefficients given by Eqs. (33)–(35). The stress $\hat{\sigma}$ of Eq. (40) is diagonalized as $\hat{\sigma}^{\rm diag}=\hat{O}^{-1}\hat{\sigma}\hat{O}$, where $\hat{O}$ is the rotation matrix, with the angle of rotation given as

$$\sin\tau=\varepsilon/(\sqrt{1+\varepsilon^2}), \tag{41}$$

where $P_2\equiv\sqrt{6P_0(3P_0+q)+(3\xi+5)(12\xi+17)F_s^2}$ and $\varepsilon=[2(3\xi+5)F_s]/(3P_0+q+P_2)$. The maximal value for τ is 33°. The elements of $\hat{\sigma}^{\rm diag}$ are $\sigma_{1,2}=[(6\xi+7)P_0-q\pm P_2]/[2(3\xi+5)]$ and $\sigma_3=P_1$. Accordingly,

$$P=\frac{9(\xi+1)P_0-2q}{3(3\xi+5)},\quad \mu=\mathcal{A}\left(\frac{3P_0+q}{2A(3\xi+5)}\right)^{1/3}, \tag{42}$$

and $\sigma_s^2=(\sigma_1-P)^2+(\sigma_2-P)^2+(\sigma_3-P)^2$. Inserting these expression into Eqs. (33)–(35) and (41), we obtain the angle τ, the Young moduli E_i, G_{12} and the Poisson ratios ν_{ij}, all as functions of $F_s/F_s^{\max}$. Neither the angle τ nor the Poisson ratios ν_{ij} depend on P_0, but all the Young moduli E_i and $G_{21}=\mu$ are proportional to $(P_0/A)^{1/3}$. These are respectively plotted (with $P_0=7.85$ kPa, $\xi=5/3$, and $\mathcal{A}=5100$ Mpa) in Fig. 8. (Note that because P_0 is a uniaxial stress, not an isotropic one, we have $E_1=118$ MPa, $E_2=E_3=86$ MPa, and $\mu=39$ MPa even for $F_s=0$.) The solid line in Fig. 7 shows the calculated $1/t\equiv E_1/E_2$ versus $u\equiv E_2/G_{12}$. As there is no data on F_s, a direct comparison is not possible, though the calculated solid curve (for small F_s) does intersect the dashed

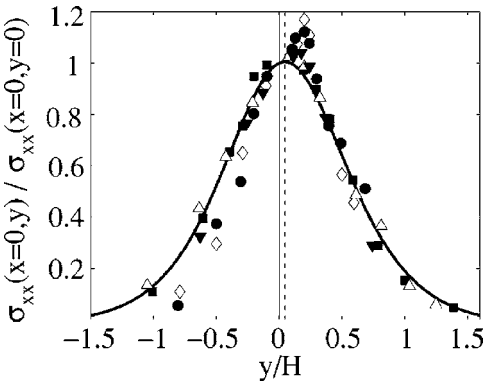

FIG. 9. Normalized pressure distribution $\sigma_{xx}(x=0,y)/\sigma_{xx}(x=0,y=0)$ at the bottom of the sheared box. Solid curve, results of numerical calculations. Dashed line is plotted through the maximum of the solid curve. It is shifted by $0.05y/H$ along the shear direction. Symbols, the experimental data extracted from Ref. [13].

one representing all points of an anisotropic elastic theory compatible with the measured tilt angle of $\beta=8°$.

Finally, we would like to mention some rather preliminary results on a numerical calculation of the total stress response to a vertical point load in the sheared box, using the software of FEMLAB. We again consider Fig. 6, or a two-dimensional layer of sand, extending from $x=0$ to $x=-H$, and from $y=0$ to $y=2L$. Force balance $\nabla_j\sigma_{ij}=\rho G_i$ is closed using the elastic-strain–stress relation of granular elasticity and solved with the boundary conditions: (i) $U_x=U_y=0$ for $x=0$, or glued at the bottom; (ii) $U_y=-\tan\alpha x$, $\sigma_{xy}=0$ for $y=0$ and $y=2L$, or uniform shear for both sides; (iii) $U_y=-H\tan\alpha$ at the top, $x=-H$, and $\sigma_{xx}=P_0$, except where the point force is, between $y=L\pm L_1$, where instead $\sigma_{xx}=P_0+P_1$ holds. In the calculation, in addition to the same values for the parameters, $\xi=5/3$ and $P_0=7.85$ kPa, we used $P_1=2P_0$, $2L=54$ cm, and $2L_1=1$ cm. The results are summarized in Fig. 9 where the normalized pressure distribution $\sigma_{xx}(x=0,y)/\sigma_{xx}(x=0,y=0)$ at the bottom of the sheared box (with the hydrostatic and background pressure, ρgH and P_0, subtracted) is shown. We see a shift of the pressure peak, with a maximal shift of $0.05y/H$, given when the maximal shear force ~ 3.27 kPa is applied. [The calculation turns instable for larger forces. Compare this value to the one obtained above, $F_s^{\max}=3.88$ kPa, see the paragraph below Eq. (40), there is a discrepancy of around 16%. This is most probably due to the choice of boundary conditions, because the stress is, even for $P_1=0$, not uniform.] The shift is well within the scatter of the data, see Fig. 9, though smaller than their mean. Calculations with $P_1=P_0$ and $P_1=3P_0$ were also done, resulting in essentially identical curves. (Because the stress of the sheared state is nonuniform, making P_1 smaller than P_0 renders the response too weak to be read off unambiguously.)

IV. SUMMARY

We employ the stress-strain relation of granular elasticity (GE), Eq. (4), already known to account for yield, volume dilatancy, shear-induced anisotropy, and stress-strain increments, to calculate the stress distribution in two classic geometries, silos and point loads. As we consider only uniform void ratio here, the two elastic coefficients are taken as $\mathcal{B}=8500$ Mpa, $\mathcal{A}=\frac{3}{5}\mathcal{B}$, and the theory is without any fit parameter. Nevertheless, we were well able to account for many measured data in these two geometries, and uncovered some interesting, perhaps even important points:

(i) The stress-strain relation of Eq. (4), is validated for the case of silos. The Janssen ratio $k_J=\sigma_{rr}/\sigma_{zz}$ is found to be spatially constant and given by the Jaky formula, $k_J=1-\sin\varphi$, where φ denotes the Coulomb angle. This demonstrates the validity of a crucial feature of GE, the fact that the yield angle φ is a relevant parameter for the stress distribution far away from yield. The industry standard of the Jaky formula is thus given a clear underpinning in physics.

(ii) When sheared granular layers are subject to a point load, measurable anisotropy results. Typically interpreted as frozen-in, it is shown to be reversible and stress induced.

[1] H. A. Janssen, Dtsch. Eng. **39**, 1045 (1895).
[2] M. Sperl, Granular Matter **8**, 59 (2006).
[3] D. O. Krimer, M. Pfitzner, K. Bräuer, Y. Jiang, and M. Liu, preceding paper, Phys. Rev. E **74**, 061310 (2006).
[4] L. Vanel and E. Clément, Eur. Phys. J. B **11**, 525 (1999); L. Vanel, P. Claudin, J. P. Bouchaud, M. E. Cates, E. Clement, and J. P. Wittmer, Phys. Rev. Lett. **84**, 1439 (2000); G. Ovarlez, C. Fond, and E. Clément, Phys. Rev. E **67**, 060302(R) (2003).
[5] G. Reydellet and E. Clément, Phys. Rev. Lett. **86**, 3308 (2001).
[6] G. Ovarlez and E. Clement, Eur. Phys. J. E **16**, 421 (2005).
[7] P. W. Rowe, Proc. R. Soc. London, Ser. A **269**, 500 (1962).
[8] P. Evesque, J. Phys. I **7**, 1501 (1997).
[9] Yimin Jiang and Mario Liu, Phys. Rev. Lett. **91**, 144301 (2003). In accordance with Ref. [10], we take $a=b=1/2$ and $\tilde{K}_b/\tilde{K}_a=4/3$ here, and use the notation $\mathcal{B}=5\tilde{K}_a/3$.
[10] Yimin Jiang and Mario Liu, Phys. Rev. Lett. **93**, 148001 (2004).
[11] R. M. Nedderman, *Statics and Kinematics of Granular Materials* (Cambridge University Press, Cambridge, 1992).
[12] D. Serero, G. Reydellet, P. Claudin, E. Clément, and D. Levine, Eur. Phys. J. E **6**, 169 (2001).
[13] A. P. F. Atman, P. Brunet, J. Geng, G. Reydellet, G. Combe, P. Claudin, R. P. Behringer, and E. Clement, J. Phys.: Condens. Matter **17** 2391 (2005).
[14] A. P. F. Atman, P. Brunet, J. Geng, G. Reydellet, P. Claudin, R. P. Behringer, and E. Clement, Eur. Phys. J. E **17**, 93 (2005).
[15] There are two situations where more than one peak may be observed, neither relevant in the present context: Either the grains are highly ordered (granular crystals), see N. W. Mueggenburg, H. M. Jaeger, and S. R. Nagel, Phys. Rev. E **66**,

031304 (2002); or the number of grains is mesoscopically small, see C. F. Moukarzel, H. Pacheco-Martinez, J. C. Ruiz-Suarez, and A. M. Vidales, Granular Matter **6**, 61 (2004); theoretical explanations and simulations are provided in C. Goldenberg and I. Goldhirsh, Nature (London) **435**, 188 (2005); and A. Kasahara and H. Nakanishi, Phys. Rev. E **70**, 051309 (2004).

[16] M. Otto, J.-P. Bouchaud, P. Claudin, and J. E. S. Socolar, Phys. Rev. E **67**, 031302 (2003).

[17] Yimin Jiang and Mario Liu, in *Powders & Grains 05*, edited by R. Garcia-Rojo, H. J. Herrmann, and S. McNamara (Belkema, Rotterdam, 2005), p. 433.

[18] G. Gudehus, in *Constitutive Relations for Soils*, edited by G. Gudehus, F. Darve, and I. Vardoulakis (Belkema, Rotterdam, 1984), pp. 3–8.

[19] M. Da Silva and J. Rajchenbach, Nature (London) **406**, 708 (2000).

[20] Considering the contact between two spherical particles, it is quite natural to assume a bulk modulus $\sim\sqrt{\Delta}$ (if shear is neglected). Considering the contact between two infinitely long cylindrical particles (something typically envisioned in two-dimensional simulations), similar considerations [see H. Poritsky, J. Appl. Mech. **17**, 191 (1950)] yield a rather different and logarithmic dependence of the bulk modulus on Δ.